https://doi.org/10.1016/j.est.2021.103629
This is the Pre-Published Version.

Process Control of Charging and Discharging of Magnetically Suspended Flywheel Energy Storage System

Biao Xiang[1], Xiang Wang[1] and Wai On Wong[2]
1, School of Mechano-Electronic Engineering, Xidian University, Xi'an 710071, China
2, Department of Mechanical Engineering, The Hong Kong Polytechnic University, Hong Kong SAR, China

Abstract

Flywheel energy storage system (FESS) is an energy conversion device designed for energy transmission between mechanical energy and electrical energy. There are high requirements on the power capacity, the charging efficiency and the output precision of FESS. Active magnetic bearings are used to suspend the flywheel (FW) rotor of the FESS in air to eliminate friction. A high rotating speed of the flywheel can increase the power capacity but it also increases the disturbance load torque on the FW rotor. An observation control model of load torque is therefore proposed to mitigate the disturbance load torque acting on magnetically suspended FESS (MS-FESS) during the charging process. Moreover, for the discharging process of MS-FESS, a compound control model combing the sliding model control and the extend state observer is proposed to improve the response speed and the output voltage precision. Simulations and experiments are conducted to testify the control performances of proposed control models during the charging and discharging processes of a MS-FESS. The charging efficiency is improved by 17.6% with 46.6% reduction of the output voltage error after using the proposed control models for the charging and discharging process control. The proposed control method has high potential to be applied for process control of charging and discharging of practical MS-FESS.

***Keywords*—flywheel energy storage system; charging process; discharging process; observation control model; compound control.**

1 Introduction

Flywheel energy storage system (FESS) [1-4] is a complicate energy storage and conversion device [5, 6]. The FESS could convert electrical energy to mechanical energy by increasing the rotating speed of flywheel (FW) rotor, so the FESS can be regarded as a motor during the charging process. On the other hand, the FESS could release the stored mechanical energy by decelerating the rotating speed and therefore the FESS could be considered as a generator during the discharging process. As an energy storage equipment, it has a series of advantages on long life span, high conversion efficiency, great energy density and tiny environmental impact. Therefore, the FESS has been widely utilized in the uninterruptable power supply system [7, 8], the power transmission system from offshore wind farm to onshore grid system [9, 10], the isolated hybrid system [11-14], the power supply system of satellite [15, 16] and the energy harvesting system of vehicle [17-19].

© 2021. This manuscript version is made available under the CC-BY-NC-ND 4.0 license http://creativecommons.org/licenses/by-nc-nd/4.0/

In order to maximize the storage capacity of FESS with constant moment of inertia and to reduce the energy loss, magnetic suspension technique is used to levitate the FW rotor to avoid the contact between the FW rotor and the stator. This kind of FESS could be classified as the magnetically suspended flywheel energy storage system (MS-FESS) [20, 21]. The friction between the FW rotor and the stator could be eliminated by levitating the FW rotor to the balanced position in air, and the position of FW rotor could be controllable in five degrees of freedom (DOFs) by regulating the magnetic forces of the magnetic suspension system [22].

In the MS-FESS, the control of charging process could affect its conversion efficiency from electrical energy to mechanical energy, and the control of discharging process determine its steady-state precision of output voltage. Therefore, a good control method for the charging and discharging processes of MS-FESS is critical for its enhancement of storage capacity and energy conversion efficiency.

A nonlinear control model based on model predictive control [23] was proposed to a FESS in presence of model uncertainties and external disturbances. Simulations were conducted to verify that the power quality of direct current (DC) link voltage was enhanced. A battery/flywheel hybrid energy storage system was used to mitigate load fluctuations in a shipboard microgrid [24]. An optimization approach and a lookup-table-based approach were proposed to outperform the baseline control in terms of power fluctuation mitigation and power loss reduction. Both the advantages and disadvantages of each strategy were analyzed. The results showed that the optimization-based method could achieve a 2% to 5% reduction in power loss in comparison to the same tracking error at nominal and high sea states. A periodic event-triggered control was designed for a FESS matrix farm in the wind power plant [25]. Simulation results indicated that the number of triggers during the power conversion process was greatly reduced and the convergence time is shortened to 0.7s. A robust discharging strategy was proposed to incorporate the speed variation to the DC-link voltage control system [26]. A speed-independent extended state observer was designed to enhance the robustness during the discharging process. Experimental results proved that the control model could accurately track the DC-link voltage from 0V to 300V. A direct voltage control strategy without intermediate current loop was designed for FESS to ensure the fast dynamic performance within its wide operation range [27]. An extended state observer was used to estimate the disturbances acting on the FESS. The experimental results implied that the maximum tracking error was reduced from 7V to 4V, and the recovery time was reduced from 0.25s to 0.1s when the FESS worked at 12000rpm. A three-layer control system including a frequency control model, a mode coordination model and a speed control mode was designed to reduce DC-link voltage variation of FESS in microgrid [28]. The settling time was shortened to 1.6s and maximum overshoot was reduced to 11V. A fuzzy proportional plus derivative control method was proposed for frequency regulation of a 2MW wind-power farm with 400kW flywheel energy storage unit [29]. The simulation results showed that the maximum frequency variation was reduced to 0.04Hz which is better than the traditional proportional plus derivative control method.

The control methods of FESS are investigated to improve the charging efficiency and the discharging precision in those above-mentioned papers, but most of them are designed for the hybrid energy storage system based on FESS. In addition, the FW rotor used in those hybrid energy storage systems are supported by mechanical bearings, and the charging and discharging processes of FESS with external disturbances are also neglected. Therefore, the charging and discharging processes of MS-FESS are worthy of being researched to improve charging efficiency and discharging precision. This article would be focused on two parts as following,

1. The charging process of the MS-FESS is investigated. A sliding mode control (SMC) method based on extended state observation (ESO) model is designed to improve the charging efficiency and robustness of the MS-FESS. The charging period is reduced from 85s to 70s through enhancing the stability of charging current.

2. The discharging process of the MS-FESS is also researched with focus on the process stability and the precision improvement of the output DC bus voltage of the MS-FESS. The error between the actual DC bus voltage and reference value is reduced from 3.28V to 1.75V when the load resistance varies.

This article is organized as follows. The structure and operational principle of the MS-FESS are introduced in section 2. A SMC based on the ESO model are designed for the charging and the discharging processes. Simulation results of the charging and discharging processes of MS-FESS with the ESO model are presented in section 3. Experimental testing results of the control performance of charging and discharging processes are presented in section 4. Finally, conclusions are drawn on the charging and discharging control of the MS-FESS.

2 The Brief Introduction about MS-FESS

2.1 The Mechanical Structure of MS-FESS

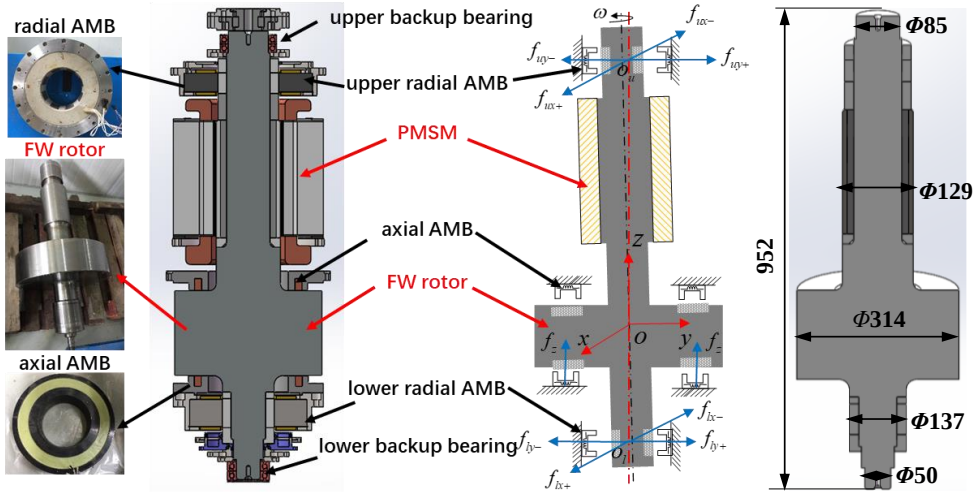

Fig. 1. The prototype of MS-FESS, (a) the components of MS-FESS, (b) the prototype of MS-FESS, (c) the suspension state of MS-FESS, (d) mechanical dimensions of flywheel rotor.

The prototype of MS-FESS is shown in Fig. 1, and the main components have a magnetic suspension system and a motor/generator system. As shown in Fig. 1(a) and (b), the magnetic suspension system including

two radial active magnetic bearing (AMB) units and an axial AMB unit. The FW rotor with a permanent magnet synchronous motor (PMSM) is suspended at the equilibrium positions in radial and axial directions. Fig. 1(c) shows the forces acting on the FW rotor. The upper and lower radial AMB generate magnetic forces to levitate the FW rotor at the radial balanced position, and the axial AMB generates magnetic forces to suspend the FW rotor at the axial equilibrium position. Moreover, the upper and lower backup bearings, as the protective devices, can restrain any excessive displacement runout of FW rotor in case of failure of the magnetic suspension system. The motor/generator system is consisted of a PMSM and a FW rotor with a large equatorial moment of inertia. The PMSM turns the rotating FW rotor around the axial principal axis during the charging process.

The MS-FESS could convert electrical energy input to mechanical energy by increasing the rotating speed of FW rotor during the charging process, and the stored energy can be written as

$$E = \frac{1}{2} J_e \omega_r^2 \tag{1}$$

where J_e is the moment of inertia of FW rotor around the axial principal axis, and ω_r is the angular velocity of the FW rotor around the axial principal axis.

The mechanical energy of the MS-FESS can be converted back to electrical energy by reducing the rotating speed during the discharging process, and the released energy could be expressed as

$$\Delta E = \frac{1}{2} J_e (\omega_{ri}^2 - \omega_{rt}^2) \tag{2}$$

where ω_{ri} is initial angular velocity of FW rotor, and ω_{rt} is terminal angular velocity of FW rotor.

2.2 The Charging Process Control of MS-FESS

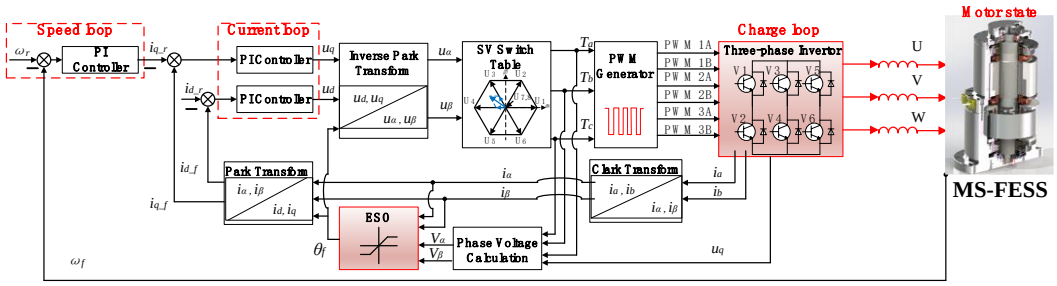

Fig. 2. The control diagram of MS-FESS during the charging process.

The MS-FESS could work at two statues including the charging and discharging processes by sharing the same three-phase invertor with different control commands. The energy of the MS-FESS is stored as mechanical energy by accelerating the FW rotor during the charging process at when the MS-FESS is working at the motor state. During the discharging process, the stored energy of the MS-FESS would be released by decelerating the rotating speed of the FW rotor, and the MS-FESS is working at the generator state.

The control diagram of the MS-FESS during the charging process is shown in Fig. 2, the energy storage is accomplished by increasing the rotating speed of FW rotor. The control models of the MS-FESS during the charging process include the speed control model and the current control model. In the speed control, a proportional integral (PI) feedback control model is used to regulate the *q*-axis current using the reference

rotating speed and the feedback speed. For the current control, a PI feedback control model is used to generate the *q*-axis control voltage combing the feedback term and the input term of *q*-axis current. Moreover, another PI feedback control is used to realize the closed-loop control of the *d*-axis current based on the feedback current. Furthermore, the space vector (SV) switch table would generate the switch signals depending on the α-axis and β-axis voltages, and the pulse width modulation (PWM) signals are then generated to control the switching sequence and the duty cycle of three-phase invertor. Finally, the three-phase voltages are output to accelerate the FW rotor in order to convert the input electrical energy to mechanical energy during the charging process.

The *d*-axis voltage and the *q*-axis voltage can be respectively expressed as

$$\begin{cases} u_d = R_s i_d + L_d \frac{di_d}{dt} - \omega_s L_q i_q \\ u_q = R_s i_q + L_q \frac{di_q}{dt} + \omega_s (L_d i_d + \psi_s) \end{cases} \tag{3}$$

where u_d is the *d*-axis control voltage, and u_q is the *q*-axis control voltage. R_s is the stator resistance. L_d is the *d*-axis equivalent inductance, and L_q is the *q*-axis equivalent inductance. i_d is the *d*-axis control current, and i_q is the *q*-axis control current. ω_s is the electromagnet angular velocity, and ψ_s is the rotor flux linkage.

The electromagnetic torque function of MS-FESS could be written as

$$\begin{cases} T_e = \frac{3P_n[\psi_s i_q + (L_d - L_q) i_d i_q]}{2} \\ T_e = T_l + B\omega_r + J_e \frac{d\omega_r}{dt} \end{cases} \tag{4}$$

where T_e is the electromagnetic torque. P_n is the number of pole pairs. T_l is the load torque, and B is the damping coefficient. The relationship between the angular velocity and the electromagnet angular velocity is written as

$$\omega_s = P_n \omega_r \tag{5}$$

In the charging process of the MS-FESS, the reference value of the *d*-axis current is defined as i_{d_r}=0. the differential equation of the *q*-axis control current and the angular velocity could be written as

$$\begin{cases} \frac{di_q}{dt} = \frac{-R_s}{L_q} i_q + \frac{1}{L_q} u_q - \frac{\psi_s}{L_q} \omega_s \\ \frac{d\omega_r}{dt} = \frac{-B}{J_e} \omega_r + \frac{1}{J_e} T_e - \frac{1}{J_e} T_l \\ T_e = \frac{3}{2} P_n \psi_s i_q \end{cases} \tag{6}$$

When the load torque of the MS-FESS is constant, the space function of the MS-FESS during the charging process could be expressed as

$$\begin{cases} \dot{\boldsymbol{x}}_c = A_c \boldsymbol{x}_c + B_c \boldsymbol{u}_c \\ \boldsymbol{y}_c = C_c \boldsymbol{x}_c \end{cases} \tag{7}$$

where the space vector $\boldsymbol{x}_c=[q_r\ \omega_r\ T_l]^{\mathrm{T}}$ (q_r is the angle position).

The input vector is $\boldsymbol{u}_c=i_q$, and the output vector is $\boldsymbol{y}_c=\omega_r$. The state matrix, the input and output matrices could be expressed respectively as

$$A_c = \begin{bmatrix} 0 & 1 & 0 \\ 0 & \frac{-B}{J_e} & \frac{-1}{J_e} \\ 0 & 0 & 0 \end{bmatrix}; \quad B_c = \begin{bmatrix} 0 \\ \frac{k_t}{J_e} \\ 0 \end{bmatrix}; \quad C_c = [0 \quad 1 \quad 0] \tag{8}$$

The state space function in (7) could be rewritten in augmented form as

$$\begin{cases} \dot{\boldsymbol{x}}_{c1} = A_{c1}\boldsymbol{x}_{c1} + B_{c1}\boldsymbol{u}_c - B_{c2}T_l \\ \boldsymbol{y}_{c1} = C_{c1}\boldsymbol{x}_{c1} \end{cases} \tag{9}$$

where $\boldsymbol{x}_{c1} = [q_r \quad \omega_r]^T$, $A_{c1} = \begin{bmatrix} 0 & 1 \\ 0 & \frac{-B}{J_e} \end{bmatrix}$, $B_{c1} = \begin{bmatrix} 0 & \frac{k_t}{J_e} \end{bmatrix}^T$, $B_{c2} = \begin{bmatrix} 0 & \frac{1}{J_e} \end{bmatrix}^T$, and $C_{c1} = [0 \quad 1]$.

The load torque is regarded as a disturbance in the charging process of the MS-FESS. The proposed ESO for the load torque could be written as

$$\dot{\tilde{\boldsymbol{x}}}_{c1} = A_{c1}\tilde{\boldsymbol{x}}_{c1} + B_{c1}\boldsymbol{u}_c - B_{c2}\tilde{T}_l + H_{c1}(C_{c1}\boldsymbol{x}_{c1} - C_{c1}\tilde{\boldsymbol{x}}_{c1}) \tag{10}$$

where those terms with the sign '~' represent the observed value of corresponding terms, and $H_{c1}=[h_1\ h_2]^T$.

The error function between the observer function in (10) and the state space function in (9) could be derived and written as

$$\dot{\boldsymbol{e}}_{c1} = \dot{\boldsymbol{x}}_{c1} - \dot{\tilde{\boldsymbol{x}}}_{c1} = (A_{c1} - H_{c1}C_{c1})\boldsymbol{e}_{c1} - B_{c2}\left(T_l - \tilde{T}_l\right) = A_e\boldsymbol{e}_{c1} - W \tag{11}$$

where $A_e = (A_{c1} - H_{c1}C_{c1})$, $W = B_{c2}\left(T_l - \tilde{T}_l\right)$ and $\boldsymbol{e}_{c1} = \boldsymbol{x}_{c1} - \tilde{\boldsymbol{x}}_{c1}$.

In order to realize an accurate observation for the load torque, the error function in (11) must be a convergence equation. According to Popov hyper-stability theory, the following two conditions must be satisfied to guarantee the convergence of the error function.

(i) $H(s)=(sI-A_e)^{-1}$ is a positive real matrix.

(ii) with $\boldsymbol{e}_y = \boldsymbol{y} - \tilde{\boldsymbol{y}}$, there is $\int_0^t \boldsymbol{e}_y^T W dt > -\gamma^2$.

Therefore, in order to ensure the error function can meet the two conditions above, the observation function of the load torque is designed and written as

$$\tilde{T}_l = \left(K_P + \frac{K_I}{s}\right)\boldsymbol{e}^T B_{c2} \tag{12}$$

where K_P is gain coefficient of estimating load torque, and K_I is integral coefficient of estimating load torque.

By expanding (11) into two equations, we have

$$s\tilde{q}_r = \tilde{\omega}_r + h_1(q_r - \tilde{q}_r) \tag{13}$$

$$s\tilde{\omega}_r = -\frac{B}{J_e}\tilde{\omega}_r - \frac{1}{J_e}\tilde{T}_l + \frac{1}{J_e}T_e + h_2(q_r - \tilde{q}_r) \tag{14}$$

Considering that $sq_r=\omega_r$, the equation (13) could be rewritten as

$$(q_r - \tilde{q}_r) = \frac{1}{s+h_1}(\omega_r - \tilde{\omega}_r) \tag{15}$$

Substituting (12) and (15) into (14), the observation function for rotating speed could be obtained and written as

$$\tilde{\omega}_r = \frac{1}{J_e+B}T_e - \frac{1}{J_e+B}\frac{1}{s+h_1}\left(\frac{K_P - {J_e}^2 h_2}{J_e} + \frac{K_I}{J_e}\frac{1}{s}\right)(\omega_r - \tilde{\omega}_r) \tag{16}$$

Compare (16) to (4), the observation function of load torque could be written as

$$\tilde{T}_l = \frac{1}{s+h_1}\left(\frac{K_P - J_e{}^2 h_2}{J_e} + \frac{K_I}{J_e}\frac{1}{s}\right)(\omega_r - \tilde{\omega}_r) \tag{17}$$

Therefore, the load torque caused by the speed error of FW rotor could be obtained.

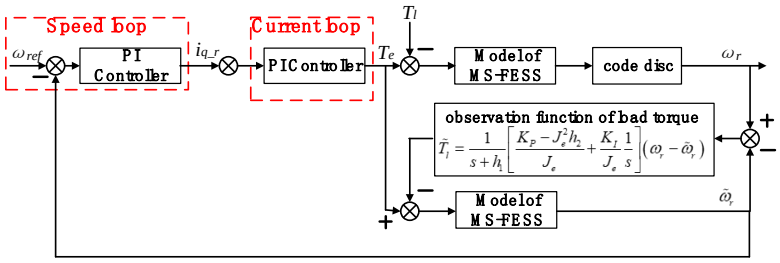

Fig. 3. The control model of MS-FESS during the charging process.

According to the above observation function design of load torque, the equivalent control model of the MS-FESS during the charging process is shown in Fig. 3. Given that the reference *d*-axis input current i_{d_r}=0, only the speed control and the *q*-axis current control are used to regulate the drive torque of MS-FESS, and ESO model of load torque is proposed to mitigate the disturbance due to load torque.

2.3 The Discharging Process Control of MS-FESS

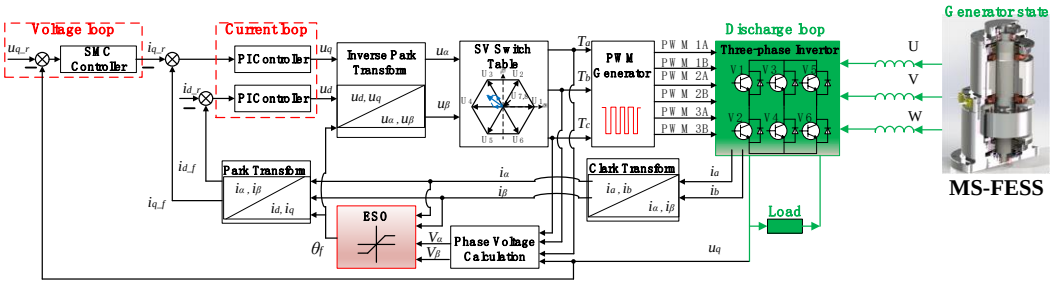

Fig. 4. The control diagram of MS-FESS during the discharging process.

When the MS-FESS is switched from the charging process to the discharging process, the reference input would be switched from the rotating speed to the reference DC bus voltage. As shown in Fig. 4, the stored mechanical energy could be converted to the electrical energy by decelerating the rotating speed of FW rotor. The back electromotive force (EMF) in three-phase windings of the MS-FESS is converted to the reference DC bus voltage through the three-phase invertor. In the discharging process of MS-FESS, a sliding mode controller (SMC) is designed for the voltage control loop with the output DC bus voltage. Furthermore, a PI controller is designed for the control loop of *q*-axis current and *d*-axis current. The PMW signals are generated to regulate the duty cycle and the on-off sequence of the discharging loop. Therefore, the discharging process of the MS-FESS would be realized.

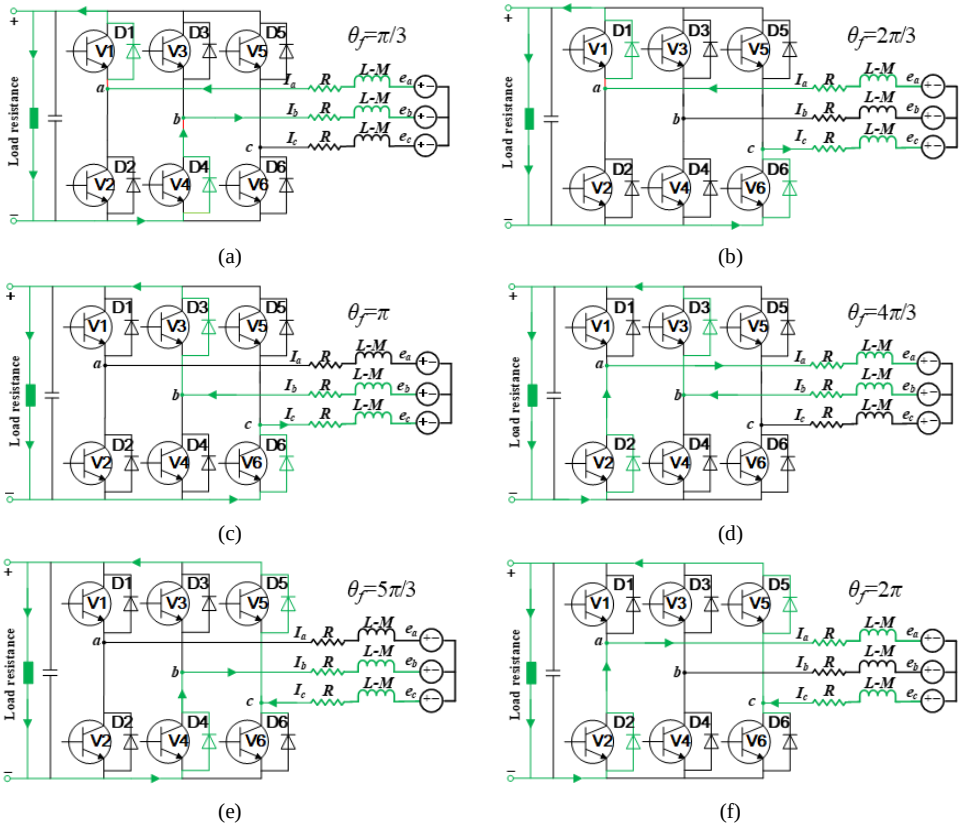

Fig. 5. The rectification models of the MS-FESS during the discharging process, (a) the electrical angle of MS-FESS is $\pi/3$, (b) the electrical angle of MS-FESS is $2\pi/3$, (c) the electrical angle of MS-FESS is π, (d) the electrical angle of MS-FESS is $4\pi/3$, (e) the electrical angle of MS-FESS is $5\pi/3$, (f) the electrical angle of MS-FESS is 2π.

For the discharging process of the MS-FESS, there are two operational modes including the passive discharging mode and the active discharging mode. For the passive discharging mode, the back EMF of the MS-FESS could be passively converted to the DC bus voltage which varies with the discharging process. The detailed discharging process with six recertification steps is shown in Fig. 5, and the current pathway is marked by the green line. During the passive discharging mode, the insulated gate bipolar transistors (IGBTs) of the three-phase invertor are switched off. The current rectification is accomplished through regulating the switch sequence of diodes. For instance, the *a*-node voltage is highest in the rectification process as shown in Fig. 5(a) with the electrical angle at $\pi/3$, and the *b*-node voltage is lowest during the first stage of passive discharging process with diode D1 and diode D4 switched on. Moreover, the current rectifications from Fig. 5(a) to (f) would be sequentially conducted when the electrical angle is increased from $2\pi/3$ to 2π in steps as shown in Fig. 5. Therefore, the current pathway would vary with the electrical angle during the rectification process.

For the active control of discharging process, the DC bus voltage acting on the load resistance is measured by the voltage sensors, and then fed back to the voltage control loop for the determination of the *q*-axis control current. Moreover, the designed ESO model could estimate the electrical angle based on phase voltages and

phase currents. Through the Clark transform and the Park transform, the phase currents i_a and i_b could be transferred to the *d*-axis feedback current i_{d_f} and the *q*-axis feedback current i_{q_f}. Through the PI controller of current control loop, the *d*-axis voltage u_d and the *q*-axis voltage u_q could be determined. The *d*-axis control voltage u_d and the *q*-axis control voltage u_q are then transferred to the α-axis control voltage u_α and the β-axis control voltage u_β through the inverse Park transform. Therefore, based on the space vectors T_a, T_b and T_c output from the switch table, the equivalent PMW sequence signals could be generated to control the switch sequence of transistors for the active discharging process.

In the feedback loop of discharging process, the feedback terms of *d*-axis and *q*-axis currents are

$$\begin{cases} i_{d\_f} = i_\alpha \cdot cos\theta_f + i_\beta \cdot sin\theta_f \\ i_{q\_f} = -i_\alpha \cdot sin\theta_f + i_\beta \cdot cos\theta_f \end{cases} \tag{14}$$

where θ_f is the electrical angle estimated by the SMC model.

To design the SMC model of voltage control loop, the equivalent α-axis and β-axis back EMFs of MS-FESS are defined as

$$\begin{cases} V_\alpha = -k_e \omega_r \, sin\theta_f \\ V_\beta = -k_e \omega_r \, cos\theta_f \end{cases} \tag{15}$$

where k_e is the back EMF coefficient. The differential functions of equivalent α-axis control current i_α and equivalent β-axis control current i_β are written as

$$\begin{cases} \frac{di_\alpha}{dt} = -\frac{R_S \cdot i_\alpha}{L_S} + \frac{V_\alpha}{L_S} + \frac{u_\alpha}{L_S} \\ \frac{di_\beta}{dt} = -\frac{R_S \cdot i_\beta}{L_S} + \frac{V_\beta}{L_S} + \frac{u_\beta}{L_S} \end{cases} \tag{16}$$

When the MS-FESS works at transition process at the rated rotating speed, there is $\frac{d\omega_r}{dt} = 0$.

The derivative functions of back EMF are

$$\begin{cases} \frac{dV_\alpha}{dt} = -\omega_r \cdot V_\beta \\ \frac{dV_\beta}{dt} = -\omega_r \cdot V_\alpha \end{cases} \tag{17}$$

So the differential functions of equivalent α-axis control current i_α and β-axis control current i_β in (16)can be rewritten as

$$\begin{cases} \frac{di_\alpha^0}{dt} = -\frac{R \cdot i_\alpha^0}{L_S} + \frac{u_\alpha - K_f z_{e\alpha} - z_\alpha}{L_S} \\ \frac{di_\beta^0}{dt} = -\frac{R \cdot i_\beta^0}{L_S} + \frac{u_\beta - K_f z_{e\beta} - z_\beta}{L_S} \end{cases} \tag{18}$$

where K_f (greater than 0) is the feedback parameter, z_α and z_β are defined as the switch functions of SMC model.

The switch functions of SMC model are expressed as

$$\begin{cases} S_\alpha = i_\alpha^0 - i_\alpha \\ S_\beta = i_\beta^0 - i_\beta \end{cases} \tag{19}$$

The switch functions of SMC model could be written as

$$\begin{bmatrix} z_\alpha \\ z_\beta \end{bmatrix} = k \cdot sat(S_{\alpha\beta}) = \begin{cases} k, & S_{\alpha\beta} > \Delta \\ \frac{kS}{\Delta}, & -\Delta < S_{\alpha\beta} < \Delta \\ -k, & S_{\alpha\beta} < -\Delta \end{cases} \tag{20}$$

where k is the control coefficient of the switch function.

Based on the Lyapunov stability, the switch function should satisfy the following condition.

$$\dot{e}_s = \dot{S}_{\alpha\beta} S_{\alpha\beta} \Rightarrow k > max(|V_\alpha| \quad |V_\beta|) \tag{21}$$

The control functions of SMC model could be designed as following

$$\begin{cases} z_{e\alpha} = \frac{z_\alpha \cdot \omega_c}{(s+\omega_c)} \\ z_{e\beta} = \frac{z_\beta \cdot \omega_c}{(s+\omega_c)} \end{cases} \tag{22}$$

where ω_c is the cutoff frequency of the low-pass filter.

The derivative equations of switch function are

$$\begin{cases} \frac{dS_\alpha}{dt} = -\frac{R \cdot S_\alpha}{L_s} + \frac{u_\alpha - K_f z_{e\alpha} - z_\alpha}{L_s} \\ \frac{dS_\beta}{dt} = -\frac{R \cdot S_\beta}{L_s} + \frac{u_\beta - K_f z_{e\beta} - z_\beta}{L_s} \end{cases} \tag{23}$$

For the stable SMC model of MS-FESS, the state lies on the sliding surface, so we get

$$\begin{cases} S_\alpha = i_\alpha^0 - i_\alpha = 0 \\ S_\beta = i_\beta^0 - i_\beta = 0 \end{cases} \tag{24}$$

Furthermore, we get

$$\begin{cases} e_\alpha = K_f z_{e\alpha} + z_\alpha \\ e_\beta = K_f z_{e\beta} + z_\beta \end{cases} \tag{25}$$

Finally, the electrical angle of FW rotor could be obtained and written as

$$\theta_f = -tan^{-1}\left(\frac{e_\alpha}{e_\beta}\right) = -tan^{-1}\left(\frac{K_f z_{e\alpha} + z_\alpha}{K_f z_{e\beta} + z_\beta}\right) \tag{26}$$

For the voltage control loop of charging process, the error function between reference voltage u_{q_r} and output voltage u_q could be expressed as

$$e_{q\_u} = u_{q\_r} - u_q \tag{27}$$

For the current control loop of charging process, the q-axis control current with PI control model could be obtained as following

$$i_{q\_r} = e_{q\_u} \cdot \left(K_{qu\_p} + K_{qu\_i} \frac{1}{s}\right) \tag{28}$$

The error function between q-axis control current and q-axis feedback current during charging process is

$$e_{q\_i} = i_{q\_r} - i_{q\_f} \tag{29}$$

The q-axis voltage u_q based on the PI control model could be expressed as

$$u_q = e_{q\_i} \cdot \left(K_{qi\_p} + K_{qi\_i} \frac{1}{s}\right) \tag{30}$$

The d-axis voltage u_d based on the PI control model is written as

$$u_d = e_{d\_i} \cdot \left(K_{di\_p} + K_{di\_i}\frac{1}{s}\right);\ s.t.\, e_{d\_i} = i_{d\_r} - e_{d\_f} \tag{31}$$

In the practical control during the active discharging process of MS-FESS, the reference *d*-axis control current is defined as i_{d_r}=0. Through on the inverse Park transform about the *d*-axis and *q*-axis control voltages, the α-axis and β-axis voltages during the discharging process can be written as

$$\begin{cases} u_\alpha = u_d \cdot cos\theta_f - u_q \cdot sin\theta_f \\ u_\beta = -u_d \cdot sin\theta_f + u_q \cdot cos\theta_f \end{cases} \tag{32}$$

Therefore, the active charging process of the MS-FESS would be realized.

3 Simulation about Charging and Discharging Process of MS-FESS

3.1 The Charging and Discharging Power Curve of MS-FESS

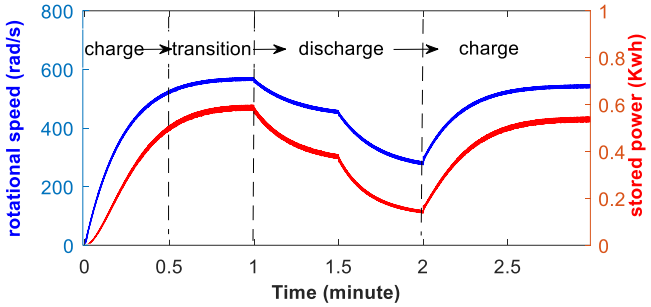

Fig. 6. The charging and discharging power curve of MS-FESS with the rotating speed.

The charging and discharging processes of MS-FESS are simulated to compare the control performances of different control models, and the relationship between the stored energy and the rotating speed during the charging process and discharging process are illustrated in Fig. 6. The stored energy is improved with the increase of rotating speed of FW rotor during the charging process. The operational status of the MS-FESS would be switched from the charging process to the transition process to maintain the rated power storage 0.5 kW·hr by keeping the rotating speed of FW rotor constant. In the discharging process, according to the reference DC bus voltage, the mechanical energy of the MS-FESS is converted to electrical energy through decelerating the rotating speed of FW rotor. When the discharging process of MS-FESS is over, the stored energy would be recharged by increasing the rotating speed of FW rotor again, and the operational mode of the MS-FESS is switched to charging mode again.

3.2 The Charging Process of MS-FESS Using ESO Model

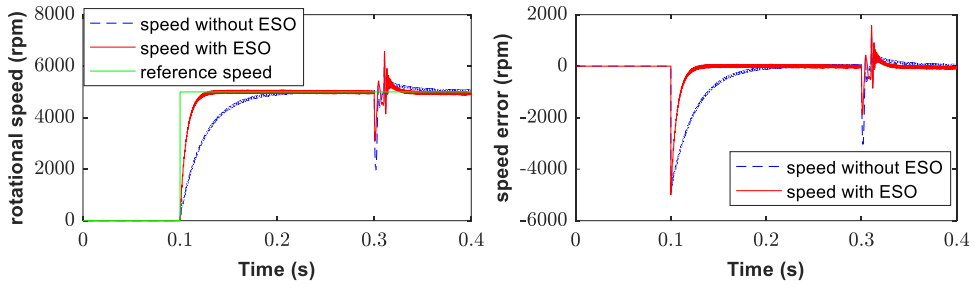

(a) (b)

Fig. 7. The speed curve of FW rotor during the charging process of MS-FESS, (a) the speed curve of FW rotor, (b) the speed error between the actual speed curve and the reference speed curve.

The speed curves and the control currents of the MS-FESS are recorded during the charging process in the simulation. The error between the actual speed and the reference speed is analyzed to verify the effectiveness of the ESO model used in the charging process. The speed curves of the MS-FESS during the charging process are plotted in Fig. 7 when the reference rotating speed is 5000 rpm. In Fig. 7(a), the actual speed of FW rotor could track the reference speed with a short time-delay. For the speed curve of the MS-FESS without using the ESO model, the time-delay is about 0.1s. However, the time delay is reduced to 0.02s after applying the ESO model. An impulse disturbance is imposed to the speed when the simulation time reaches to 0.3s. The speed error response of the FW rotor is shown in Fig. 7(b). The maximum speed error without using the ESO model is about 3000rpm at the response point, and it is reduced to 2000rpm after the ESO model is applied. Simultaneously, the control currents i_q and i_d of the MS-FESS during the charging process are recorded and they are plotted in Fig. 8. For the q-axis control current i_q as shown by the blue line in Fig. 8(a), the maximum variation of the q-axis current i_q reaches to 14.1A without the ESO model, and it is reduced to 11.7A after applying the ESO model which is about 17% difference between the two cases. Fig. 8(b) shows the curves of the d-axis current i_d, the obvious variation of the d-axis current i_d occurs when the speed curve of MS-FESS varied from the rated value, but the deflection magnitudes of d-axis current i_d without and with the ESO model are quite close.

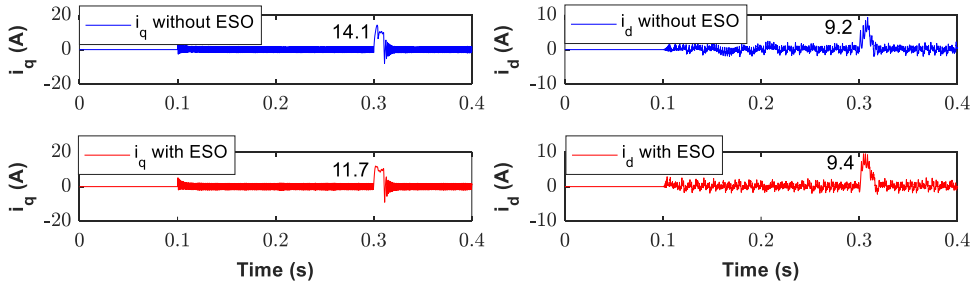

(a) (b)

Fig. 8. The control current curves during the charging process of MS-FESS, (a) the q-axis current i_q curve of MS-FESS, (b) the d-axis current i_d curve of MS-FESS.

3.3 The Discharging Process of MS-FESS Using SMC Model

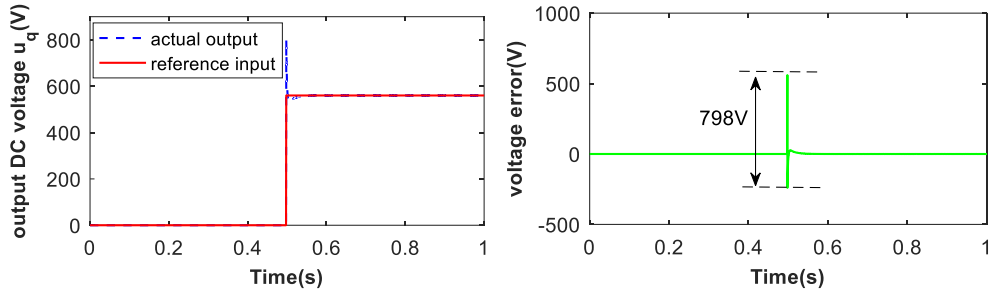

(a) (b)

Fig. 9. (a) The DC bus voltage curve during the discharging process of MS-FESS, (b) the voltage error between the actual output DC bus voltage and the reference input DC bus voltage during the discharging process of MS-FESS.

The discharging process of MS-FESS is also investigated by simulation. The DC bus voltage and the control currents of MS-FESS are compared and analyzed. Firstly, the DC bus voltages during the discharging process are recorded and plotted in Fig. 9(a) with the reference DC bus voltage sets at 560V. There is a short time-delay between the reference voltage and the actual output voltage. The DC bus voltage is hold at the stable amplitude 560V during the discharging process. As shown in Fig. 9(b), the maximum error between the reference input DC bus voltage and the actual output DC bus voltage is about 798V due to the time delay of the speed control loop and the current control loop. The *d*-axis and *q*-axis current curves of the ME-FESS during the discharging process are recorded and plotted in Fig. 10 to verify the tracking performance of the SMC model. As shown in Fig. 10(a), although the *q*-axi current i_q has an obvious oscillation at the initial discharging moment, the *q*-axis current i_q of the MS-FESS varies within the stable range [-5A 5A] during the discharging process. On the other hand, the *d*-axis current i_d during the discharging process jumps to a negative value -22A when the MS-FESS is switched to the discharging process as shown in Fig. 10(b). The MS-FESS is then working at the field-weakening operation process. The *d*-axis current i_d oscillates stably with a small amplitude during the discharging process of the MS-FESS.

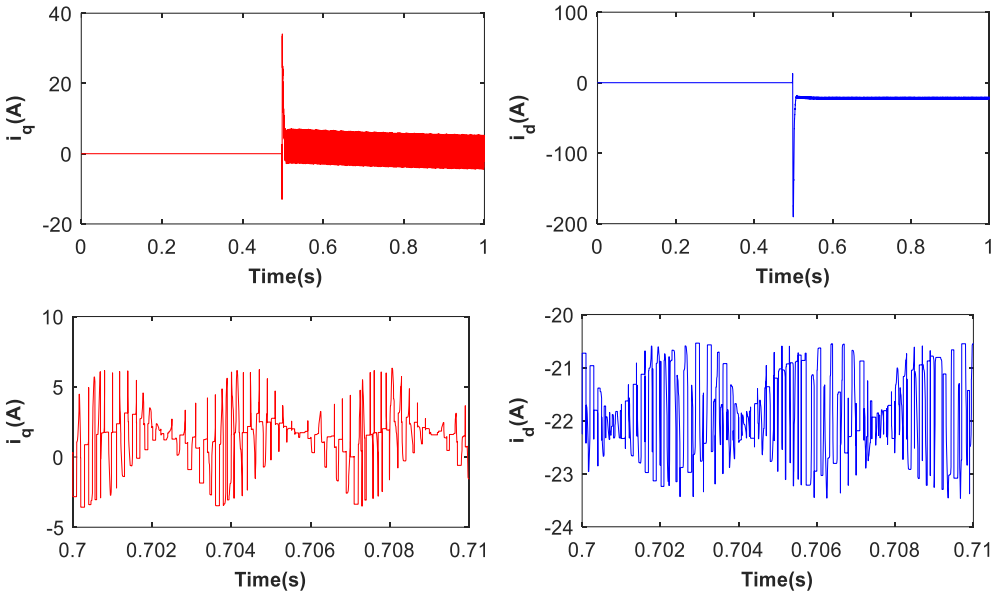

(a) (b)

Fig. 10. The *d*-axis and *q*-axis current curves during the discharging process of MS-FESS, (a) the *q*-axis current curve during the discharging process of MS-FESS, (b) the *d*-axis current curve during the discharging process of MS-FESS.

Above all, for the charging process of the MS-FESS, the designed ESO model could accurately estimate the disturbance acting on the speed regulation process, and the variations of the control current and the rotating speed of the FW rotor could be effectively suppressed. For the discharging process of the MS-FESS, the control model could exactly track the reference input DC bus voltage, and the control currents of the ME-FESS are maintained within stable ranges.

4 Charging and Discharging Experiment of MS-FESS

4.1 Experimental Setup of MS-FESS

The experimental setup of MS-FESS is shown in Fig. 11. The major components include a PMSM rotor system, a magnetic suspension system, a charging/discharging system, a control system and a measurement system. The PMSM could govern the rotating speed of FW rotor to realize operational switching of the charging and the discharging processes. A pump is used to provide vacuum inside to mitigate the wind resistance at high rotating speed. The magnetic suspension system has two couples of radial AMB units at upper end and lower end are used to control the radial translations and tilting of FW rotor. The axial translation of FW rotor is controlled by two couples of axial AMB units at upper side and lower side of FW rotor's disc, so the friction between the FW rotor and the stator could be avoided. In the charging and discharging system of the MS-FESS, the three-phase inverting and rectifying system is composed of three couples of IGBT units, three couples of rectifier diodes and a voltage conversion module, and the charging/discharging process of the MS-FESS could be realized by the inverting/rectifying system based on the proposed control methods as described before. The control system is based on a DSP+FPGA control chip for signal processing and code programming. In addition,

a data acquisition (DAQ) module and the displacement sensors form the measurement system to collect the current and voltage signals of the MS-FESS and the dynamic displacements of FW rotor during the charging and discharging processes. The industrial PC (IPC) and the oscilloscope (OSC) monitor the system status of the MS-FESS. The detailed system parameters of the MS-FESS are listed in

TABLE. I, and the control parameters of the MS-FESS during the charging and discharging processes are listed in TABLE II.

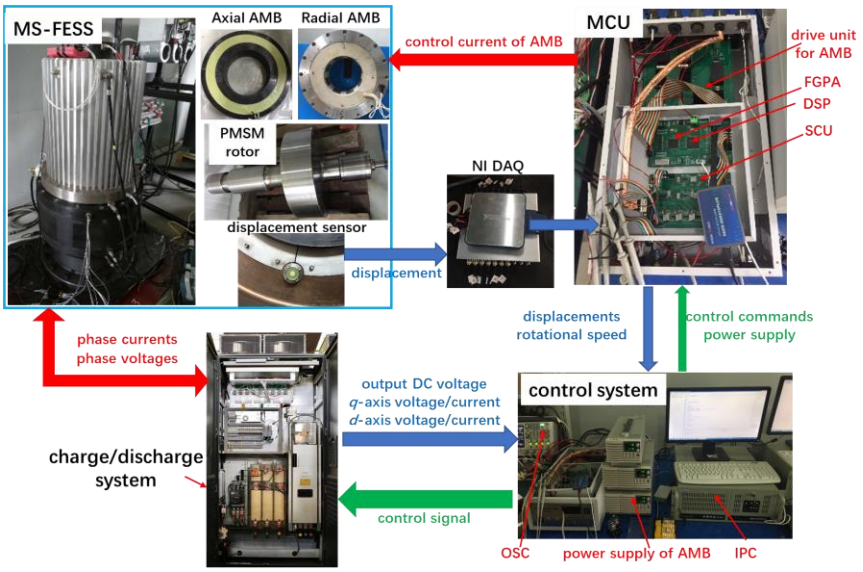

Fig. 11. The whole experimental setup of MS-FESS.

TABLE. I. The system parameters of MS-FESS.

Setup	Attributes
PMSM/FW rotor system	mass m=150Kg torque coefficient k_t=0.54 back-EMF coefficient k_e=0.065 rotor flux linkage ψ_s=0.18Wb stator resistance R=0.24Ω stator flux inductance L_d=L_q=0.08mH equatorial moment of inertia J_e=1.459Kgm^2 rotating speed ω=5000rpm pole pairs p_n=2 material of FW rotor 35CrMnSiA
Magnetic suspension system	radial displacement stiffness -2800N/mm axial displacement stiffness -1700N/mm radial current stiffness 620N/A axial current stiffness 470N/A power consumption at steady-state 147W

	power consumption during suspension 188W
Charging/Discharging system	Self-designed system IGBT: CM35MXA-24S Diode: RM600DY-34S
Control system	DSP: TMS320F28335 FPGA: Altera EPF10K30RC208 power supply system: Tektronix Keithley
Measurement system	sensitivity of displacement sensor 3.3V/mm DAQ Board: NI PCI 6355 Oscilloscope: Keysight 2000 X-Series

TABLE. II. The control parameters of MS-FESS during charging and discharging processes.

Symbol	Quantity	Value
h_1	parameter of ESO	0
h_2	parameter of ESO	1.5×10^3
K_p	gain coefficient of ESO	1.1
K_I	integral coefficient of ESO	0.02
k	control parameter of SMC model	65
K_f	feedback coefficient of SMC model	1
ω_c	cutoff frequency of low-pass filter	1000Hz
K_{qu_p}	proportional coefficient of q-axis voltage	0.8
K_{qu_i}	integral coefficient of q-axis voltage	22
K_{qi_p}	proportional coefficient of d-axis voltage	9.6
K_{qi_i}	integral coefficient of d-axis voltage	24

4.2 The Control Performance of Magnetic Suspension System

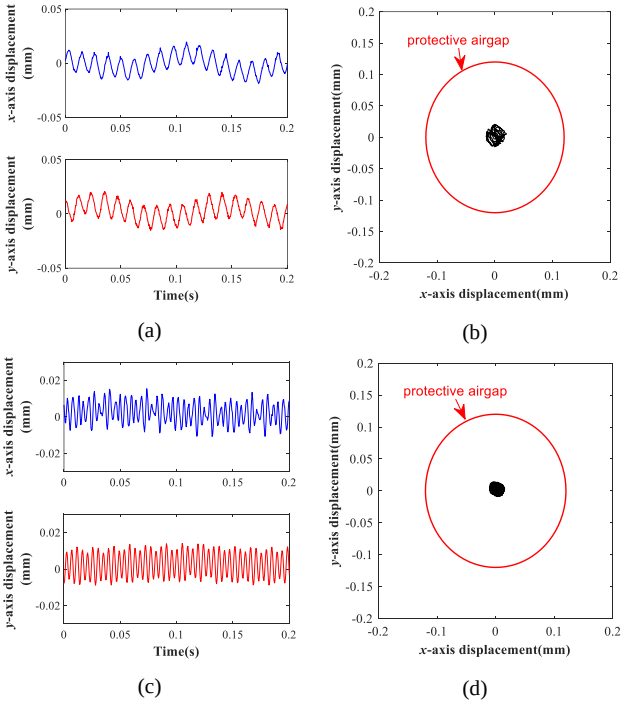

Fig. 12. The suspension performances of magnetic suspension system, (a) dynamic displacements of flywheel rotor at 5000rpm, (b) axis orbit of flywheel rotor at 5000rpm, (c) dynamic displacements of flywheel rotor at 12000rpm, (b) axis orbit of flywheel rotor at 12000rpm.

The magnetic suspension system is the critical unit of MS-FESS, the suspension performance is tested first. When the rotational speed of flywheel rotor is 5000rpm, the dynamic displacements of flywheel in *x* and *y* axis are shown in Fig. 12(a), the max displacement is 0.02mm which is 16.7% of the 0.12mm protective airgap. The axis orbit of flywheel rotor at 5000rpm is plotted in Fig. 12(b), and it shows that the flywheel rotor can be stably suspended within the protective airgap. Moreover, when the rotational speed of flywheel rotor is 12000rpm, the dynamic displacements in *x* and *y* axes are illustrated in Fig. 12(c). The max displacement is 0.01mm which is only 8.4% of the protective airgap. The axis orbit of flywheel rotor is plotted in Fig. 12(d). It shows that the flywheel rotor is stably suspended within the protective airgap. Moreover, the power of magnetic suspension system during the suspension process is 187.54W, and the power at steady suspension state is 146.88W.

4.3 The Energy Storage Curves of MS-FESS During Charging and Discharging Processes

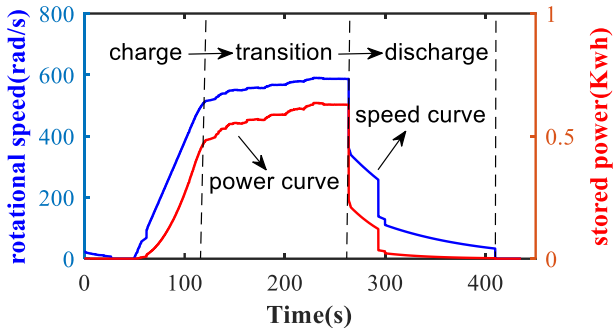

Fig. 13. The relationship between the stored energy and the rotating speed during the charging and discharging processes of MS-FESS.

In this part of experiment, the power storage curves of the MS-FESS during the charging and discharging processes are recorded and plotted in Fig. 13. The rotating speed of the MS-FESS is shown by the blue line while the stored power of the MS-FESS during the charging and discharging processes is displayed by the red line. The working process of the MS-FESS could be divided into three processes including the charging process, the transition process and the discharging process. When the MS-FESS is working in the charging mode, the stored energy raises with the increase of rotating speed, and its rated value is 0.5kW·h at 5000rpm. Furthermore, the operation of the MS-FESS would be switched from the charging mode to the transition or the holding mode when the rotating speed kept at the rated value. During the discharging process of the MS-FESS, the stored energy would rapidly fall to the set point by decelerating the rotating speed, so the stored energy can be released as electrical energy. Therefore, the fast switches among different operational modes could be realized, and the charging and discharging process of the MS-FESS could be accomplished by storing of the mechanical energy and releasing to electrical energy.

4.4 The Charging Control Process of MS-FESS Using ESO Model

The charging performance of the MS-FESS is tested on the rotor acceleration and the control current variations during the charging process. The charging period and the stability of control current are shown to be

the critical parameters of the charging process. The control currents of the MS-FESS during the charging and discharging processes with and without the proposed ESO control model are plotted in Fig. 14(a) and (b), respectively. In both cases, the q-axis control current i_q of the MS-FESS is regulated to 80A to accelerate the rotating speed of FW rotor during the charging process to convert the electrical energy to mechanical energy. The control current shows much bigger fluctuations in Fig. 14(a). The control currents are varied in a stable range in both cases after the rotating speed of FW rotor reaches the rated value and the control mode is switched to maintain the speed of FW rotor in the transition process.

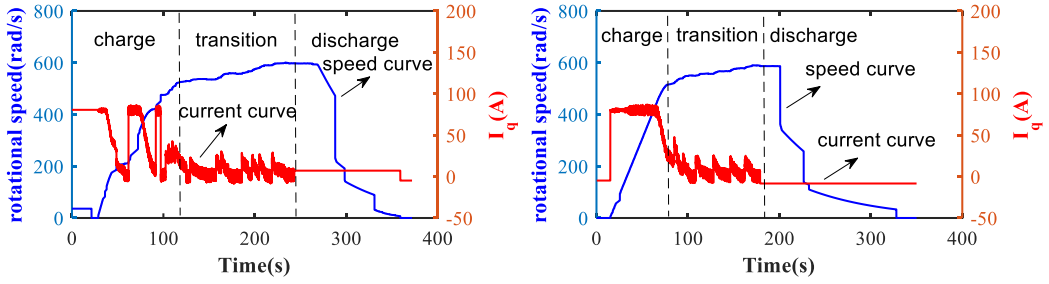

Fig. 14. The control currents of MS-FESS during the charging and discharging process, (a) the control currents of the MS-FESS without the ESO model, (b) the control currents of the MS-FESS with the ESO model.

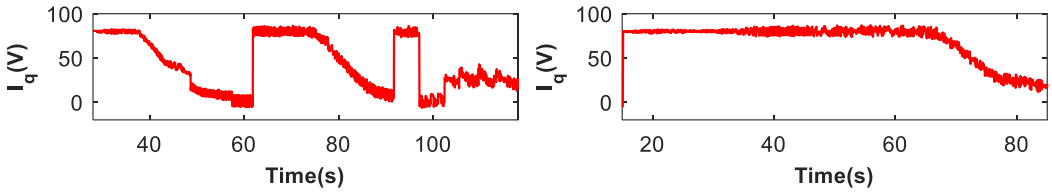

Fig. 15. The control current curve during the charging process of the MS-FESS, (a) the control current curve of the MS-FESS without the ESO model, (b) the control current curve of the MS-FESS with the ESO model.

The q-axis control currents of the MS-FESS during the charging process are shown in Fig. 15 to compare the charging performance of different control models. For the q-axis current curve without the ESO control model in Fig. 15(a), there are large fluctuations of the control current about the reference current 80A during the charging process, and therefore the acceleration of the FW rotor during the charging process is affected and it takes a longer acceleration period during charging as shown in Fig. 14(a). On the other hand, the q-axis current curve with the ESO model as shown in Fig. 15(b) can be maintained at the set value 80A with just very small variations. As a result, the charging period of the MS-FESS with the ESO model is greatly shortened from 85s into 70s.

4.5 The Discharging Control Process of MS-FESS Using SMC Model

Moreover, the precision of output DC bus voltage is the most important parameter to the discharging process, and the robustness of discharging process is also critical when the load resistance varies. The speed curve and the output DC bus voltage of the MS-FESS during the discharging process are measured for testing

of the proposed control method for discharging. The measured output DC bus voltage curves with and without using the SMC model are plotted in Fig. 16(a) and (b), respectively. The output DC bus voltages of the MS-FESS in both cases vary with the rotating speed during the charging process and the transition process, and it is maintained at the steady-state amplitude by tracking the reference value during the discharging process. The error between the actual output DC bus voltage and the reference input DC voltage (560V) during the discharging process of the ME-FESS with and without using the SMC model are plotted in Fig. 17(a) and (b), respectively. The root mean square (RMS) value of voltage error is used as an index to evaluate the control performance of the MS-FESS during the discharging process. For the voltage error without the SMC model in Fig. 17(a), the RMS of output DC bus voltage during the discharging process is 3.28V while it is reduced to 1.75V after using the SMC model as shown in Fig. 17(b). The relative reduction is 46.6% after applying the SMC model in the control of the discharging process of the MS-FESS.

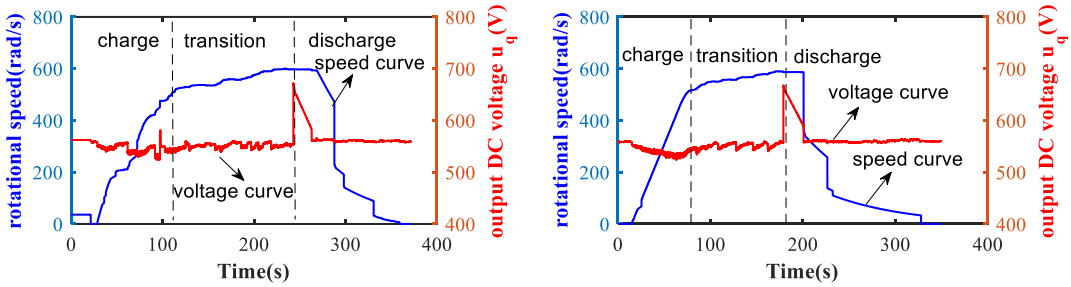

Fig. 16. The output DC bus voltage during the charging and discharging processes of the MS-FESS, (a) the output DC bus voltage of the MS-FESS without the SMC model, (b) the output DC bus voltage of the MS-FESS with the SMC model.

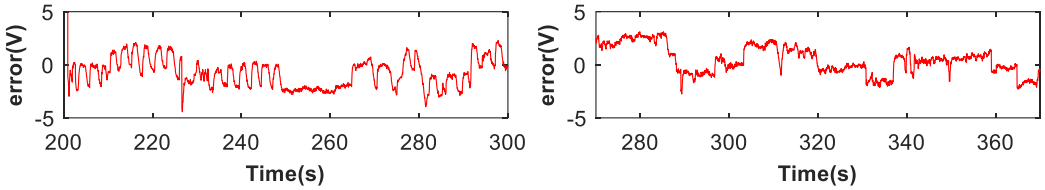

Fig. 17. The output voltage error during the discharging process of MS-FESS, (a) the voltage error of MS-FESS without the SMC model, (b) the voltage error of the MS-FESS with the SMC model.

Above all, the experimental tests show that the proposed ESO control model can improve the charging performance of the MS-FESS by accurately tracking the control current for accelerating the rotating speed of the FW rotor. Moreover, the proposed SMC control model can reduce the voltage error between the actual output DC bus voltage and the reference voltage during the discharging process of the MS-FESS.

5 Conclusion and Discussion

The charging and discharging processes of MS-FESS are analyzed in this article. An ESO control model is proposed to improve the charging speed of the MS-FESS and a SMC control model is proposed to reduce the voltage error during the discharging process of the MS-FSS. In the charging process of the MS-FESS with the

proposed ESO model, the reference speed curve of the MS-FESS is more accurately tracked. The acceleration period of charging process is reduced from 85s to 70s, so the ESO model could significantly improve the efficiency and robustness of the MS-FESS during the charging process. Moreover, for the discharging process of the MS-FESS, the voltage error between the actual value and the reference voltage is reduced by 46.6% with the designed SMC model. The test results show that the proposed SMC model can significantly improve the output precision of DC bus voltage.

In the future work, the charging and discharging process of MS-FESS with higher rotational speed will be investigated, and the combination of several MS-FESS will be considered to improve the energy storage. Moreover, other control methods would be designed for the MS-FESS to improve the overall system performance.

Acknowledgement

The authors would like to thank The Hong Kong Polytechnic University of Hong Kong for the support of this research (ref: 16900506R).

Conflict of Interest Statement

The authors declare no conflict of interest in preparing this article.

References

[1] F. Faraji, A. Majazi, and K. Al-Haddad, "A comprehensive review of flywheel energy storage system technology," *Renewable and Sustainable Energy Reviews*, vol. 67, pp. 477-490, 2017.
[2] E. Elbouchikhi, Y. Amirat, G. Feld, M. Benbouzid, and Z. Zhou, "A Lab-scale Flywheel Energy Storage System: Control Strategy and Domestic Applications," *Energies*, vol. 13, no. 3, p. 653, 2020.
[3] J. P. Rouse, S. D. Garvey, B. Cárdenas, A. Hoskin, L. Swinfen-Styles, and W. Xu, "A case study investigation into the risk of fatigue in synchronous flywheel energy stores and ramifications for the design of inertia replacement systems," *Journal of Energy Storage*, vol. 39, p. 102651, 2021/07/01/ 2021.
[4] O. Aydogmus, G. Boztas, and R. Celikel, "Design and analysis of a flywheel energy storage system fed by matrix converter as a dynamic voltage restorer," *Energy*, vol. 238, p. 121687, 2022/01/01/ 2022.
[5] A. Kailasan, T. Dimond, P. Allaire, and D. Sheffler, "Design and analysis of a unique energy storage flywheel system—An integrated flywheel, motor/generator, and magnetic bearing configuration," *Journal of Engineering for Gas Turbines and Power*, vol. 137, no. 4, p. 042505, 2015.
[6] B. Xiang and W. Wong, "Power Compensation Mechanism for AMB System in Magnetically Suspended Flywheel Energy Storage System," *Measurement*, p. 108646, 2020.
[7] W. Gengji and W. Ping, "Rotor loss analysis of PMSM in flywheel energy storage system as uninterruptable power supply," *IEEE Transactions on Applied Superconductivity*, vol. 26, no. 7, pp. 1-5, 2016.
[8] X. Li, B. Anvari, A. Palazzolo, Z. Wang, and H. Toliyat, "A utility-scale flywheel energy storage system with a shaftless, hubless, high-strength steel rotor," *IEEE Transactions on Industrial Electronics*, vol. 65, no. 8, pp. 6667-6675, 2017.
[9] M. I. Daoud, A. M. Massoud, A. S. Abdel-Khalik, A. Elserougi, and S. Ahmed, "A flywheel energy storage system for fault ride through support of grid-connected VSC HVDC-based offshore wind farms," *IEEE Transactions on Power Systems*, vol. 31, no. 3, pp. 1671-1680, 2015.
[10] N. S. Gayathri, N. Senroy, and I. N. Kar, "Smoothing of wind power using flywheel energy storage system," *IET Renewable Power Generation*, vol. 11, no. 3, pp. 289-298, 2016.
[11] A. Saleh, A. Awad, and W. Ghanem, "Modeling, control, and simulation of a new topology of flywheel energy storage systems in microgrids," *IEEE Access*, vol. 7, pp. 160363-160376, 2019.

[12] J. Hou, J. Sun, and H. Hofmann, "Control development and performance evaluation for battery/flywheel hybrid energy storage solutions to mitigate load fluctuations in all-electric ship propulsion systems," *Applied energy*, vol. 212, pp. 919-930, 2018.
[13] A. K. Arani, H. Karami, G. Gharehpetian, and M. Hejazi, "Review of Flywheel Energy Storage Systems structures and applications in power systems and microgrids," *Renewable and Sustainable Energy Reviews*, vol. 69, pp. 9-18, 2017.
[14] S. Ghosh and S. Kamalasadan, "An Energy Function-Based Optimal Control Strategy for Output Stabilization of Integrated DFIG-Flywheel Energy Storage System," *IEEE Transactions on Smart Grid*, vol. 8, no. 4, pp. 1922-1931, 2017.
[15] V. Lappas, D. Richie, C. Hall, J. Fausz, and B. Wilson, "Survey of technology developments in flywheel attitude control and energy storage systems," *Journal of guidance, control, and dynamics*, vol. 32, no. 2, pp. 354-365, 2009.
[16] A. Rupp, H. Baier, P. Mertiny, and M. Secanell, "Analysis of a flywheel energy storage system for light rail transit," *Energy*, vol. 107, pp. 625-638, 2016.
[17] N. B. binti Ahamad, C.-L. Su, X. Zhaoxia, J. C. Vasquez, J. M. Guerrero, and C.-H. Liao, "Energy harvesting from harbor cranes with flywheel energy storage systems," *IEEE Transactions on Industry Applications*, vol. 55, no. 4, pp. 3354-3364, 2019.
[18] S. R. Gurumurthy, V. Agarwal, and A. Sharma, "A novel dual-winding BLDC generator–buck converter combination for enhancement of the harvested energy from a flywheel," *IEEE Transactions on Industrial Electronics*, vol. 63, no. 12, pp. 7563-7573, 2016.
[19] B. Thormann, P. Puchbauer, and T. Kienberger, "Analyzing the suitability of flywheel energy storage systems for supplying high-power charging e-mobility use cases," *Journal of Energy Storage*, vol. 39, p. 102615, 2021/07/01/ 2021.
[20] C.-S. Toh and S.-L. Chen, "Design, modeling and control of magnetic bearings for a ring-type flywheel energy storage system," *Energies*, vol. 9, no. 12, p. 1051, 2016.
[21] B. Xiang and W. on Wong, "Vibration characteristics analysis of magnetically suspended rotor in flywheel energy storage system," *Journal of Sound and Vibration*, vol. 444, pp. 235-247, 2019.
[22] T. Wen, B. Xiang, and S. Zhang, "Optimal control for hybrid magnetically suspended flywheel rotor based on state feedback exact linearization model," *Science Progress*, vol. 103, no. 3, p. 0036850420951389, 2020.
[23] M. Ghanaatian and S. Lotfifard, "Control of Flywheel Energy Storage Systems in the Presence of Uncertainties," *IEEE Transactions on Sustainable Energy*, vol. 10, no. 1, pp. 36-45, 2019.
[24] J. Hou, Z. Song, H. Hofmann, and J. Sun, "Control Strategy for Battery/Flywheel Hybrid Energy Storage in Electric Shipboard Microgrids," *IEEE Transactions on Industrial Informatics*, vol. PP, no. 99, pp. 1-1, 2020.
[25] Y. Sun, J. Hu, and J. Liu, "Periodic event-triggered control of flywheel energy storage matrix systems for wind farms," *IET Control Theory & Applications*, vol. 14, no. 11, pp. 1467-1477, 2020.
[26] X. Zhang and J. Yang, "A Robust Flywheel Energy Storage System Discharge Strategy for Wide Speed Range Operation," *IEEE Transactions on Industrial Electronics*, vol. 64, no. 10, pp. 7862-7873, 2017.
[27] X. Zhang and J. Yang, "A DC-Link Voltage Fast Control Strategy for High-Speed PMSM/G in Flywheel Energy Storage System," *IEEE Transactions on Industry Applications*, vol. 54, no. 2, pp. 1671-1679, 2018.
[28] M. S. Mahdavi, G. B. Gharehpetian, and H. A. Moghaddam, "Enhanced Frequency Control Method for Microgrid-Connected Flywheel Energy Storage System," *IEEE Systems Journal*, pp. 1-11, 2020.
[29] J. Yao, M. Yu, W. Gao, and X. Zeng, "Frequency regulation control strategy for PMSG wind-power generation system with flywheel energy storage unit," *IET Renewable Power Generation*, vol. 11, no. 8, pp. 1082-1093, 2017.